



## RESEARCH ARTICLE OPEN ACCESS

# Triphase Heterogeneous Electrocatalysts of Ni and Co for High-Performing Li-O<sub>2</sub> Batteries

Shadeepa Karunaratne<sup>1</sup> | Chanaka Sandaruwan<sup>2</sup> | Yasun Y. Kannangara<sup>2</sup> | Denisa Demko<sup>3</sup> | François Orange<sup>4</sup> | Alice Mija<sup>5</sup> | Ali Reza Kamai<sup>6,7</sup>  | Amr M. Abdelkader<sup>1</sup> 

<sup>1</sup>Faculty of Science and Technology, Bournemouth University, Talbot Campus, Poole, UK | <sup>2</sup>Sri Lanka Institute of Nanotechnology, Homagama, Sri Lanka | <sup>3</sup>Electrical Engineering Division, Department of Engineering, University of Cambridge, Cambridge, UK | <sup>4</sup>Université Côte d'Azur, Centre Commun de Microscopie Appliquée (CCMA), Nice, France | <sup>5</sup>Université Côte d'Azur, ICN, France | <sup>6</sup>Energy and Environmental Materials Research Centre (E2MC), Key Laboratory for Ecological Metallurgy of Multimetallic Mineral, Ministry of Education, Northeastern University, Shenyang, China | <sup>7</sup>Department of Materials Science and Metallurgy, University of Cambridge, Cambridge, UK

**Correspondence:** Shadeepa Karunaratne ([skarunaratne@bournemouth.ac.uk](mailto:skarunaratne@bournemouth.ac.uk)) | Ali Reza Kamai ([a.r.kamali@cantab.net](mailto:a.r.kamali@cantab.net)) | Amr M. Abdelkader ([aabdelkader@bournemouth.ac.uk](mailto:aabdelkader@bournemouth.ac.uk))

**Received:** 20 September 2024 | **Revised:** 13 December 2024 | **Accepted:** 22 January 2025

**Funding:** This work was supported by the French government, through the UCAJ.E.D.I. Investments in the Future project managed by the National Research Agency (ANR), ANR-15-IDEX-01.

**Keywords:** discharge product modulation | Li-O<sub>2</sub> battery | Li<sub>2</sub>O<sub>2</sub> orientation | sheet-like growth | triphase heterogeneous electrocatalysts

## ABSTRACT

The limited energy density of the current Li-ion batteries restricts the electrification of transportation to small- and medium-scale vehicles. On the contrary, Li-O<sub>2</sub> batteries (LOBs), with their significantly higher theoretical energy density, can power heavy-duty transportation, if the sluggish electrode kinetics in these devices can be substantially improved. The use of solid electrocatalysts at the cathode is a viable strategy to address this challenge, but current electrocatalysts fail to provide sufficient discharge depths and cyclability, primarily due to the formation of the film-like discharge product, Li<sub>2</sub>O<sub>2</sub>, on catalytic sites, which obstructs charge transport and gas diffusion pathways. Here, we report that a triphase heterogeneous catalyst comprising NiCoP, NiCo<sub>2</sub>S<sub>4</sub>, and NiCo<sub>2</sub>O<sub>4</sub>, assembled into a hierarchical hollow architecture (NC-3@Ni), efficiently modulates the morphology and orientation of the discharge product, facilitating the sheet-like growth of Li<sub>2</sub>O<sub>2</sub> perpendicular to the cathode surface. These modifications enable the assembled LOB to deliver a high discharge capacity of 25 162 mAh g<sup>-1</sup> at 400 mA g<sup>-1</sup>, along with impressive cycling performance, achieving 270 cycles with a discharge depth of 1000 mAh g<sup>-1</sup>, exceeding 1350 h of continuous operation. This promising performance is attributed to the presence of individual electrophilic and nucleophilic phases within the heterogeneous microstructure of the triphase catalyst, collectively promoting the formation of sheet-like Li<sub>2</sub>O<sub>2</sub>.

## 1 | Introduction

The evolution of high-performing secondary batteries is a necessity for achieving sustainable goals such as electrifying transportation [1]. Uprising metal-sulfur [2] and metal-air batteries [3] with superior capacity retention capabilities have the potential to make these goals more realistic. Among them, Li-air (or Li-O<sub>2</sub>) batteries received significant attention due to their extraordinary theoretical energy density of 11.6 kWh kg<sup>-1</sup> [4].

Nevertheless, this is challenging to achieve the theoretical capacity due to certain complexities, despite years of promising research. Sluggish oxygen kinetics at the battery cathode and the parasitic reactions were identified as the major culprits hindering the performance of Li-O<sub>2</sub> batteries (LOBs) [5].

During the LOB discharge in an aprotic medium, O<sub>2</sub> from the environment diffuses into the battery and reacts electrochemically with Li ions at the surface of the cathode, forming an

This is an open access article under the terms of the [Creative Commons Attribution](https://creativecommons.org/licenses/by/4.0/) License, which permits use, distribution and reproduction in any medium, provided the original work is properly cited.

© 2025 The Author(s). *EcoMat* published by The Hong Kong Polytechnic University and John Wiley & Sons Australia, Ltd.

intermediate solid product of  $\text{LiO}_2$  [6]. The intermediate product has a high tendency to disproportionately form the final product of  $\text{Li}_2\text{O}_2$ , while a second electrochemical reduction or the stabilization of the intermediate product at the defective sites of the cathode cannot be completely ruled out [7]. However, the structural properties and the crystallinity of the discharged product rely upon the features of the electrolyte and the cathode. Solid electrocatalysts integrated cathodes with high affinity to intermediate discharge products are known to support the surface-mediated mechanism, allowing the film-like growth of  $\text{Li}_2\text{O}_2$ , covering the surface of the cathode [7]. On the contrary, electrolytes with high donor number (mostly with redox mediators) facilitate the  $\text{LiO}_2$  diffusion into the electrolyte, forming toroid-shaped  $\text{Li}_2\text{O}_2$ , generally known as the solution-mediated process. Despite achieving high discharge capacities, LOBs operating under solution-mediated processes are commonly suffocating with higher charging overpotentials and extended exposure to singlet oxygen upon charging as  $\text{Li}_2\text{O}_2$  toroids are loosely in contact with the cathode, reducing the lifespan of the batteries [8]. Similarly, batteries with solid electrocatalysts suffer from limited discharge capacity as the film-like growth of  $\text{Li}_2\text{O}_2$  is fast passivating the cathode surface [9]. Hence, it is crucial to identify strategies that could control the structural and morphological properties of the  $\text{Li}_2\text{O}_2$ , enabling faster and prolonged oxygen kinetics, and facilitating the achievement of high discharge capacity as well as extended cyclability.

Recently, many strategies were developed toward optimizing the catalytic properties of bifunctional electrocatalysts suitable for promoting both oxygen reduction reaction (ORR) that occurs during the LOB discharge, and oxygen evolution reaction (OER), which helps to evolve the oxygen out from the battery through the decomposition of the discharged intermediates during the charging step [10]. Special efforts were made to optimize the d-orbital electron occupancy of transition metal compounds promoting the adsorption of  $\text{O}_2$  and intermediate discharge products on the catalyst surface facilitating faster oxygen kinetics. Synthesis of binary multivalent compounds with optimized stoichiometry [11], heteroatom doping [12], alloying [13], high-index facet growth [14, 15], and hybrid structures [16] are some of the recently studied techniques for altering the electronic structure of catalysts, resulting in improved LOB performances. Synthesis of hybrid catalysts with heterogeneous phases is identified as an effective strategy in redistributing the surface electron structure in electrocatalysts, well-backed by the density functional theory calculations-based theoretical studies [17]. The heterogeneous phases are known to generate in-built electric fields across the interfaces due to differences in conductivity, and provide voltage gradient across the interface, promoting the redistribution of the electron densities following the Faraday law [18]. Within the structure, certain phases with relative electron deficiencies could act as electrophilic domains promoting oxygen evolution, attracting the intermediate oxygen compounds, and facilitating an efficient decomposition of the discharged product, while the electron-rich neighboring domains could facilitate the oxygen reduction by acting as nucleophilic domains [19]. The abrupt electron transfer through the different domains reduces the coulombic losses, and the reversing of the fields and the generation of secondary electronic fields is also possible during the operation to facilitate the fast charge transfer [20]. Studies conducted by Peng et al. [21] and Liang et al. [22] with dual-phase

heterogeneous catalysts already benefited from the optimized electronic properties yield discharged capacities of 10050 mAh  $\text{g}^{-1}$  at 200 mA  $\text{g}^{-1}$  and 3530 mAh  $\text{g}^{-1}$  at 600 mA  $\text{g}^{-1}$ , respectively. The study by Yan et al. with NiO and NiP phases on Ni foam further solidified the theoretical understanding of the working mechanism of the electrocatalyst with heterogeneous phases, while delivering decent battery performances [16]. Recent studies [22, 23] suggest that the interfaces between heterogeneous phases of binary transition metal compounds can be highly effective in promoting durable and rapid electrode kinetics, thereby enhancing the performance of LOBs.

Advancing from homogeneous and dual-phase heterogeneous catalytic compounds, in this study, we synthesized a versatile tri-phase heterogeneous electrocatalytic structure comprising binary phases of oxide, sulfide, and phosphide of Ni and Co. The interactions between heterogeneous phases, namely  $\text{NiCo}_2\text{O}_4$ , NiCoP, and  $\text{NiCo}_2\text{S}_4$ , along with electron transfer between their valence states, are found to be critical for the success of the resulting cathodes in LOBs. This modified catalytic structure provides a suitable environment to promote the formation of sheet-like discharge products, growing into the electrolyte while well attached to the surface of the cathode. The morphology and orientation of  $\text{Li}_2\text{O}_2$  support the battery to achieve an impressive initial specific discharge capacity of 25162 mAh  $\text{g}^{-1}$  at 400 mA  $\text{g}^{-1}$ , allowing the continuous diffusion of  $\text{Li}^+$  ions on the catalytic surface through the vertically growing pillars of  $\text{Li}_2\text{O}_2$  during the discharge. In addition to suitable catalytic properties, the direct contact between  $\text{Li}_2\text{O}_2$  and the catalytic sites enables the swift decomposition of the discharge products achieving extended cycle durability with 270 cycles at 400 mA  $\text{g}^{-1}$  under a limited discharge depth of 1000 mAh  $\text{g}^{-1}$ , exceeding 1350 h of continuous operation. The hollow microspherical structure of the catalytic particles was also beneficial toward achieving superior gravimetric capacities. Furthermore, the bottom-up grown self-assembled hierarchical network of catalytic structures on the Ni foam was supportive in achieving lower ohmic resistances as well as protecting the cathode from potential nucleophile attacks, allowing a highly efficient and durable operation of the assembled LOBs.

## 2 | Chemicals and Methods

### 2.1 | Synthesis of Catalytic Structures

Catalysts were synthesized by a two-step process, involving a hydrothermal step to form intermediate phases, followed a sulfidization/phosphorization step to fabricate the final catalysts. The hydrothermal process was conducted in a well-sealed semi-filled Teflon-lined autoclave vessel to achieve the in situ growth of catalytic microstructures on the inserted Ni foam. For this, the Ni foam was cleaned thoroughly with a deionized (DI) water/ethanol mixture to remove the surface pollutants using an ultrasonic bath cleaner (Elmasonic Easy 10 H, 37 kHz), followed by etching out of the surface oxide layer by dipping in a diluted HCl/ $\text{HNO}_3$  for 3–4 h, before rinsing with DI water. The nutrient solution for the hydrothermal reaction was prepared by adding metal salts of 2.5 mmol  $\text{Ni}(\text{NO}_3)_2 \cdot 6\text{H}_2\text{O}$  and 5 mmol  $\text{Co}(\text{NO}_3)_2 \cdot 6\text{H}_2\text{O}$  with 10 mmol of urea into 100 ml DI water and continuously stirring the mixture for 4 h until the dispersed salts are fully dissolved in water.

In a typical synthesis, 70 mL of the nutrient solution was added along with a vertically placed Ni foam in the autoclave chamber, and the hydrothermal vessel was heated to 120°C at a 5°C/min rate. After enabling the crystal growth for 12 h at 120°C, the vessel was cooled down at the same rate, and pink-gray colored hydrothermal product coated on the Ni foam was collected once the vessel reached room temperature. The loosely attached particles on the intermediate catalyst-coated Ni foams were removed by placing them in the ultrasonic bath for several minutes. The foams were further washed with DI water and dried overnight at 120°C before further processing, and the intermediate catalytic product is labeled as NC-OH@Ni for future reference.

The intermediate catalytic structures were placed downstream in a horizontal tube furnace (CARBOLITE CTF 12) with equally weighted  $\text{NaH}_2\text{PO}_2 \cdot \text{H}_2\text{O}$  and thiourea placed upstream. The partial phosphorization and sulfurization were achieved by heating the intermediate phases at 400°C for 3 h while maintaining a steady Ar flow. A constant temperature gradient of 5°C/min was maintained during both the heating and cooling phases of the calcination process, and the final catalyst (NC-3@Ni) was collected and kept under inert conditions. For comparison, NCS@Ni and NCP@Ni catalytic cathodes were prepared by replacing the upstream material with excessive amounts of thiourea and  $\text{NaH}_2\text{PO}_2 \cdot \text{H}_2\text{O}$ , respectively, while NCO@Ni was prepared by opening the chamber to air without any upstream precursor while keeping the other process conditions same. Figure 1 presents a graphical illustration of the synthesis process.

## 2.2 | Material Characterization

Morphological and dimensional properties of the in-situ synthesized catalytic microstructures were analyzed using a scanning electron microscope (SEM; HITACHI SU6600, JEOL JSM-6700F). The same technique was later used during the discharge/charge

product analysis. The crystalline phases present in the synthesized catalytic structures and the discharged products were analyzed using an x-ray diffraction microscope (XRD; Siemens D5000 with  $\text{Cu K}\alpha$ ). X-ray photoelectron spectroscopy (XPS; ESCALB 250Xi Thermo Fisher, USA) was used to understand the surface chemical composition and to determine the redistribution of the surface electronic structure due to the formation of the heterostructure. The analysis was carried out in the constant analyzer energy mode by exposing the samples to a 2000 eV ion beam (sourced from an Al  $\text{K}\alpha$  target) for 30 s with a 900  $\mu\text{m}$  spot size. Thermo Advantage Version V5.9931 software was used for the detailed spectral processing and the charge compensation effects were corrected by offsetting the binding energy relative to the intrinsic aliphatic component of the C1s spectrum to 284.8 eV. Further analysis of the nanocrystalline catalytic structures was carried out using a transmission electron microscope (TEM, JEOL JEM-2100, JEOL JEM-1400), and the high-resolution TEM images were further processed by GATAN DigitalMicrograph software to determine the reveal the crystallographic phases present in the catalytic heterostructures. The samples' specific surface area and porosity characteristics were measured using the Quanta Chrome Autoflow (BET) instrument using Barrett-Joyner-Halenda (BJH) mode.

## 2.3 | Electrochemical Studies

Electrochemical measurements were conducted using the assembled meshed CR2032-type LOB cells. All batteries were assembled inside an Ar-filled glove box and during the assembly, Li metal chip, celguard 2500 membrane, and 13 mm diameter-sized disks of synthesized catalytic Ni foam were used as the anode, separator, and cathode of the battery, respectively, while 1 M LiTFSI in tetraethylene glycol dimethyl ether (TEGDME) was used as the battery electrolyte. Active material mass-loading in the catalytic cathodes was varied from 0.8 to 1.1  $\text{mg cm}^{-2}$ , and all freshly assembled LOBs were allowed to reach their equilibrium

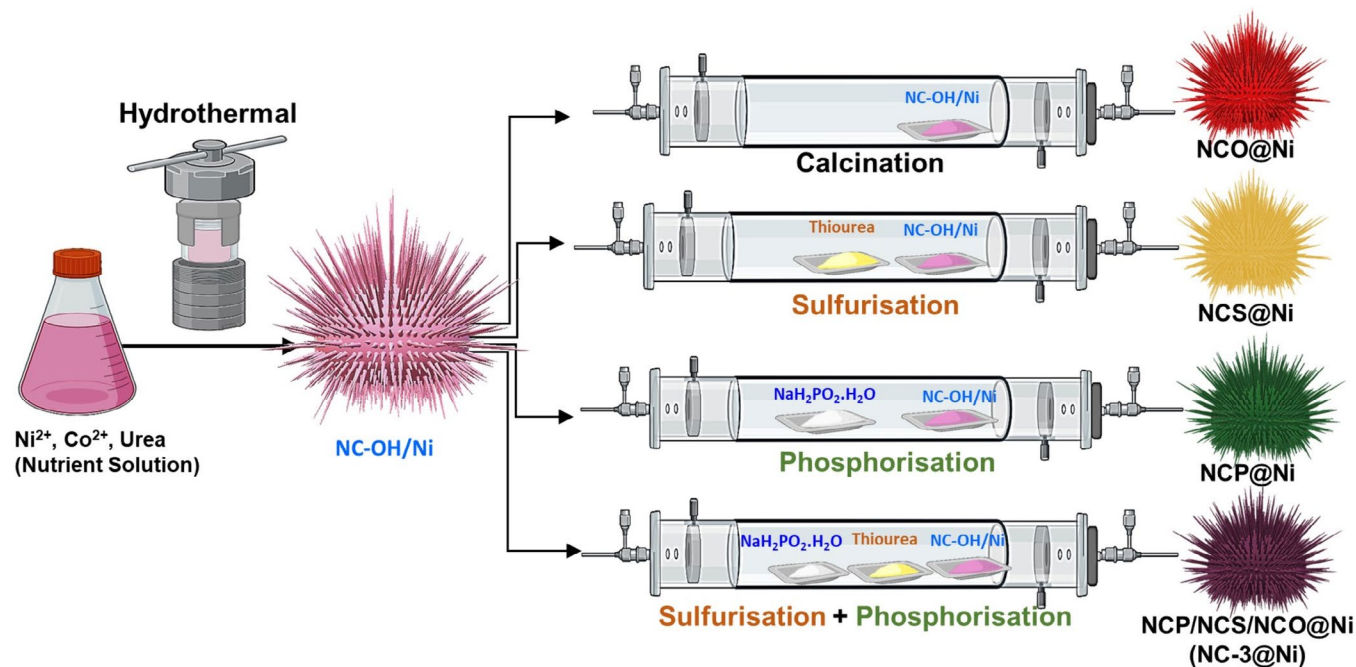


**FIGURE 1** | Schematic representation of the procedure used for the preparation of electrocatalysts.

conditions before conducting any electrochemical analysis by keeping them in an O<sub>2</sub>-filled sealed container for 12 h under atmospheric pressure.

Catalytic performances of the as-synthesized catalysts integrated cathode structures were analyzed using cyclic voltammetry (CV) studies, which were conducted in a potential window of 2.0–4.5 V versus Li/Li<sup>+</sup> at a scan rate of 0.2 mV/s, using IviumStat system. A 5 mV sinusoidal signal in the frequency range of 1 MHz–0.01 Hz was used for the electrochemical impedance spectroscopy (EIS) analysis and the resultant spectrums were fitted for an equivalent electrical circuit representing the referred electrochemical system. Galvanostatic charge/discharge (GCD) analysis was used to determine the discharge/charge capacity, cycle stability, and rate performances of the assembled LOB cells. A Neware battery analyzer was used for all GCD studies. Current densities ranging from 100 to 800 mA g<sup>-1</sup> were used during the analysis. The amount of active materials present in the individual cathodes was considered while determining the corresponding current densities and the specific capacities.

### 3 | Results and Discussion

The synthesis of the network of specifically shaped 3D microstructures was achieved by hydrothermal synthesis, where the used hydrothermal conditions helped to form the obtained spherical morphology, and further details on synthesizing specific crystal morphologies via controlling the nucleation and the growth conditions can be found in our previous articles [11, 24]. As illustrated in Figure 1, hydrothermal synthesis was used as the first step of catalytic particle synthesis. In-situ phosphorization and sulphurization were conducted in parallel during the second step to achieve both phosphide and sulfide phases in the final catalytic product of NC-3@Ni, and the full conversion to either phosphide or sulfide phases was avoided by using a limited quantity of the phosphorous and sulfur sources in the upstream during the calcination.

During the hydrothermal synthesis, unidirectional crystal growth was noticed, where the formed individual nanoneedles assembled into groundsel flower-like microspheres. Furthermore, the individual microspheres were self-assembled hierarchically on the Ni foam as presented in Figure S1. The particle shapes and the morphological features remain similar in the final catalyst as well, where the hierarchically grafted catalytic structures with 3–5 μm diameter were observed in the final catalyst of NC-3@Ni as depicted in Figure 2a,b. It is noteworthy to mention that the catalytic microstructures were found to be hollow (see Figure 2c,d), and Figure 2d provides a graphical overview of the 3D cross-section of an individual catalyst particle. Unlike Li-ion batteries, a hollow core is beneficial for LOB in obtaining high specific capacities, since only the catalytic sites present at the surface of the cathode partake in the reaction process. The surface morphology of the catalytic cathode is also pivotal in achieving higher discharge capacities since the mesoporous surface structure with a high surface area could provide a well-suited space to accumulate large quantities of the discharge products, and the NC-3@Ni catalytic particles with 71.18 m<sup>2</sup> g<sup>-1</sup> BET surface area representing the type IV isotherm and H3 hysteresis characteristic behavior (see Figure S2) consist

with adequate surface properties promoting higher discharge capacities. The energy-dispersive x-ray mapping of the catalyst surface confirms the presence of Ni-Co, P, S, and O elements on the surface with an approximate ratio of 7:4:6 between the respective phases of NiCo<sub>2</sub>O<sub>4</sub>, NiCo<sub>2</sub>S<sub>4</sub>, and NiCoP. The study further verified the uniform distribution of the elements over the surface of the synthesized microstructures as depicted in Figure 2e.

The catalytic structures provided weak X-ray diffraction signals due to their nanocrystalline nature. Hence the catalyst particles detached from the Ni foam substrate were used during the XRD analysis to obtain a higher clarity. The XRD analysis presented in Figure 3a indicates the existence of multiple heterogeneous crystal phases in the final catalyst. The peak positions of 2θ = 40.25°, 45.02°, 47.57°, 54.42°, 66.45°, and 72.92° are closely overlapped with the peak structure in JCPDS# 071-2336 which are assignable to (111), (201), (210), (002)/(300), (310), and (212) phases of NiCoP, while the peaks found at 2θ = 26.79°, 34.23°, 37.85°, 51.18°, 56.63°, 62.63°, and 78.39° provide evidence of the presence of the binary cubic spinel structure of NiCo<sub>2</sub>S<sub>4</sub> (JCPDS# 020-0782). Overlapping of the remaining peaks of the XRD spectra at 2θ = 35.75°, 38.79°, 45.02°, 60.36°, and 77.47° with the peak structure of JCPDS# 020-0781 indicates the presence of NiCo<sub>2</sub>O<sub>4</sub> as well in the synthesized heterogeneous catalytic structure.

The TEM image in Figure 3b shows the assembly of nanoclusters forming into petal-like nanoneedles which are further assembled into hierarchical hollow spheres. High-resolution TEM (HRTEM) studies helped to realize that individual nanoclusters were comprised of phosphide, sulfide, and oxide facets of Ni and Co as depicted in Figures 3f,g and S3. As demonstrated in Figure 3c, the identified lattice fringes with an interlayer distance of 0.21 nm correspond with the (111) characteristic facet of NiCoP [25]. Similarly, the crystal facets with 0.25 and 0.30 nm are assignable to the (311) phases of NiCo<sub>2</sub>O<sub>4</sub> [24] and NiCo<sub>2</sub>S<sub>4</sub> [26], respectively. The realization of the co-existence of three heterogeneous phases (typically with different binding energies to O<sub>2</sub> and intermediate discharge products) is critical in understanding the discharging and charging mechanisms of the LOB. Placing a limited quantity of NaH<sub>2</sub>PO<sub>2</sub> · H<sub>2</sub>O and thiourea upstream during the calcination is pivotal in achieving partial phosphorization and partial sulphurization, and the remaining portions of the material were converted to metal oxide phases as observed during both XRD and HRTEM studies. The XPS studies analyzed interactions between the identified heterogeneous domains.

XPS studies presented in Figure 4 were used to identify the elemental composition and the interaction between different elements in the synthesized NC-3@Ni. The high-resolution XPS spectra were also studied for comprehensive understanding of the chemical states of elements in the sample. Mechanically separated catalyst particles were used during the experiment and the survey spectra depicted in Figure 4a identify the presence of Ni-Co, O, S, and P elements on the surface of the heterogeneous catalyst of NC-3. The spectra detect the presence of C, which could be sourced from the contaminations or adventitious carbon. The deconvoluted Ni 2p high-resolution narrow band spectra of NC-3@Ni and NCO@Ni are shown in Figure 4b, and both samples are well-fitted into spin doublets with shake-up satellite

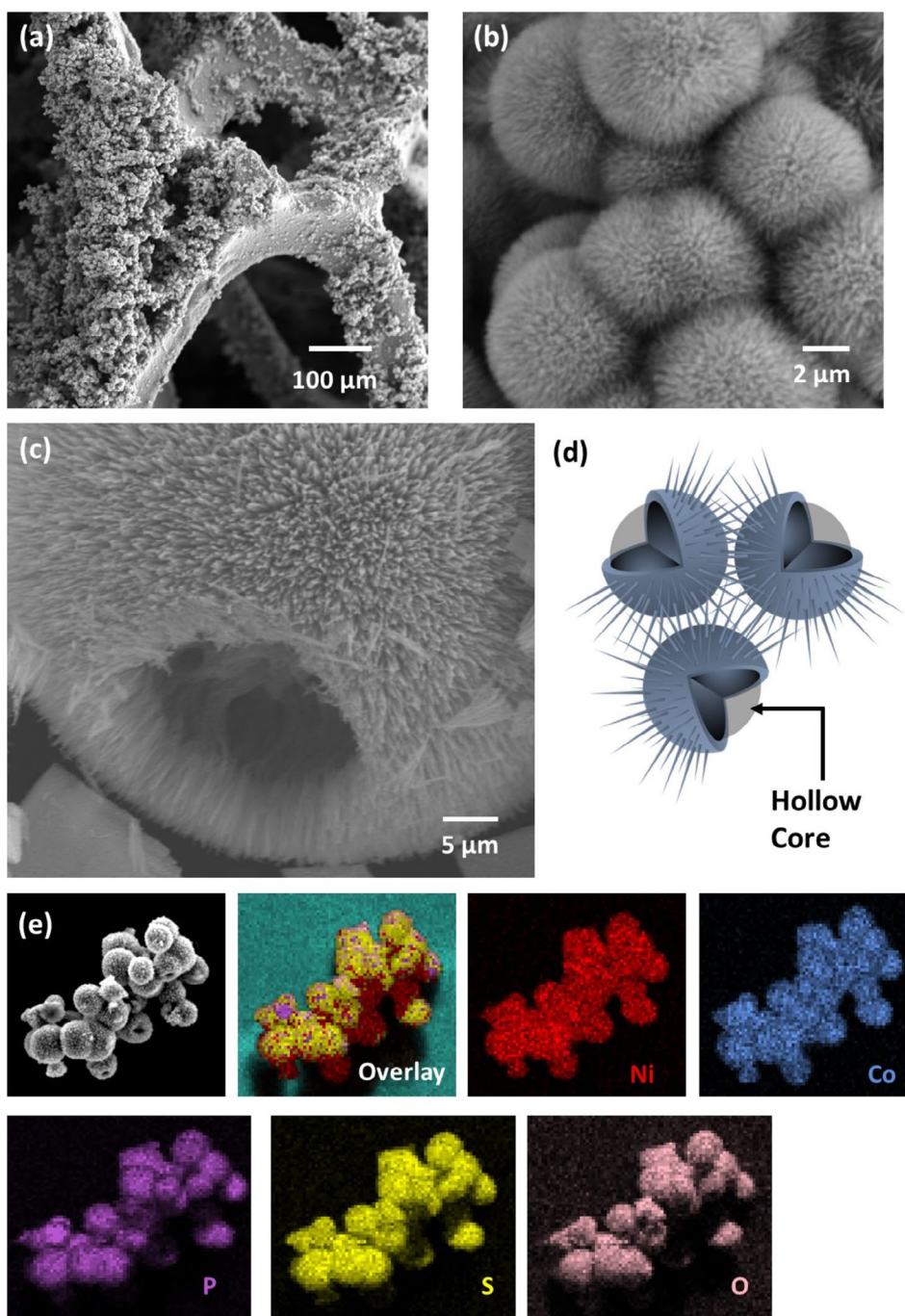


**FIGURE 2** | (a–c) SEM images, (d) graphical illustration of the hollow core, (e) EDX elemental mapping of the NC-3@Ni catalyst structure.

peaks.  $\text{Ni}^{2+}$  and  $\text{Ni}^{3+}$  valences related to Ni  $2p_{3/2}$  were positioned at 853.7 and 855.2 eV, respectively, in NCO/Ni [11]. However, a significant shift in the binding energies was observed with  $\text{Ni}^{2+}$  red shifting by 1.0–852.7 eV, while  $\text{Ni}^{3+}$  was blue-shifted by 1.2–856.4 eV in the heterogenous catalyst of NC-3@Ni. Considerable shifts in binding energies indicate the presence of other Ni-involved chemical phases and possible interactions between the phases. Similar observations were made during Co 2p spectral analysis. Co 2p spectra can also be deconvoluted into well-fitted spin doublets and related shakeup peaks. The  $\text{Co}^{2+}$  valance of Co  $2p_{3/2}$ , originally placed at 779.4 eV for NCO@Ni, was moved by 0.3 eV toward higher binding energies in the NC-3@Ni (see Figure 4c), supplementing the observations made on Ni 2p

spectra. The presence of P was identified in the heterogeneous catalyst during the P 2p spectral analysis (see Figure 4d), and as commonly observed during XPS analysis of metal phosphides, surface phosphide phases were oxidized in contact with atmospheric air [27]. It was observed that the phosphate peak shifted toward higher binding energies (133.2 eV) in the heterostructure compared with the peak position in the pure phosphide phase (132.8 eV), indicating electron transfer from the phosphide phase to neighboring oxide or sulfide phases. The higher binding energies in the phosphate phase reflect the influence of stronger bonds in adjacent insulating oxide or sulfide phases, contributing to the overall electronic modulation within the heterostructure [28]. Figure 4e presents O 1s spectra, and three peaks O1,

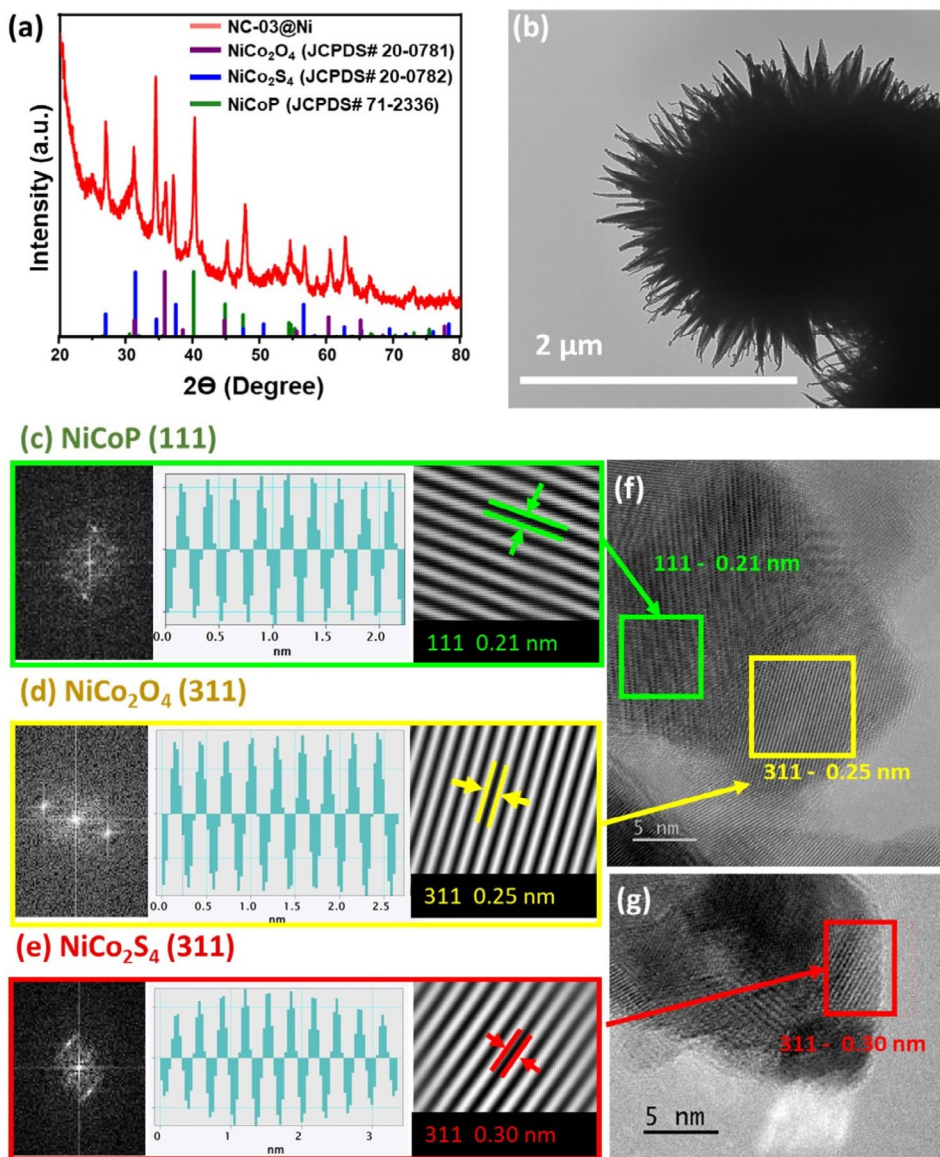


**FIGURE 3** | (a) XRD spectra, (b) TEM image, (c) identified 111 facet of NiCoP, (d) identified 311 facet of NiCo<sub>2</sub>O<sub>4</sub>, (e) identified 311 facet of NiCo<sub>2</sub>S<sub>4</sub> from the HRTEM images (f, g) of the heterogeneous catalyst of NC-3@Ni.

O<sub>2</sub>, and O<sub>3</sub> represent lattice oxygen, low oxygen coordination sites/P—O bond or S—O bond (further confirmed in S 2p spectra in Figure 4f), and surface adsorbed hydroxyl groups in water molecules, respectively [28]. The figure provides strong evidence of chemical modification on the catalytic surface structure upon the conducted in situ phosphorization and sulfurization. Compared with the pure oxide phase, the O<sub>1</sub>/O<sub>2</sub> peak ratio is substantially reduced in the heterogeneous structure of NC-3@Ni, suggesting significantly fewer lattice-oxygen bonds of metal oxide domains are presented in the heterogeneous structure implying the successful phosphorization [29] and sulfurization [30, 31]. Moreover, the binding energy of the lattice-oxygen bond shifted by 0.4 eV toward a lower value of 529.3 eV (compared with its position on the pure metal oxide phase), providing further evidence of interactions of Ni-Co oxide phases with neighboring Ni-Co sulfide and Ni-Co phosphide phases. Overall, the XPS studies confirm the presence of Ni-Co oxide, Ni-Co sulfide, and Ni-Co phosphide heterogeneous phases in the synthesized catalytic microstructure. These shifts in binding energies suggest

strong interphase interactions, where the electronic structure of NC-3@Ni is effectively modulated by charge redistribution between the heterogeneous phases.

### 3.1 | Electrochemical Analysis

All electrochemical analyses for the derived catalytic structures were conducted using assembled CR2032-type meshed LOB coin cells. The disks cut into 13 mm diameter of the NC-3-integrated catalyst heterostructure on the Ni foam were used as the binder-free cathode, while Li foil, celgard 2400 membrane, and 1 M LiTFSI in TEGDME were used as the anode, separator, and the electrolyte of the battery, respectively. LOBs assembled with NCO@Ni, NCS@Ni, and NCP@Ni were used for the comparative analysis.

As presented in Figure 5a, CV studies were used to analyze the electrocatalytic activity of the catalytic cathodes, which were

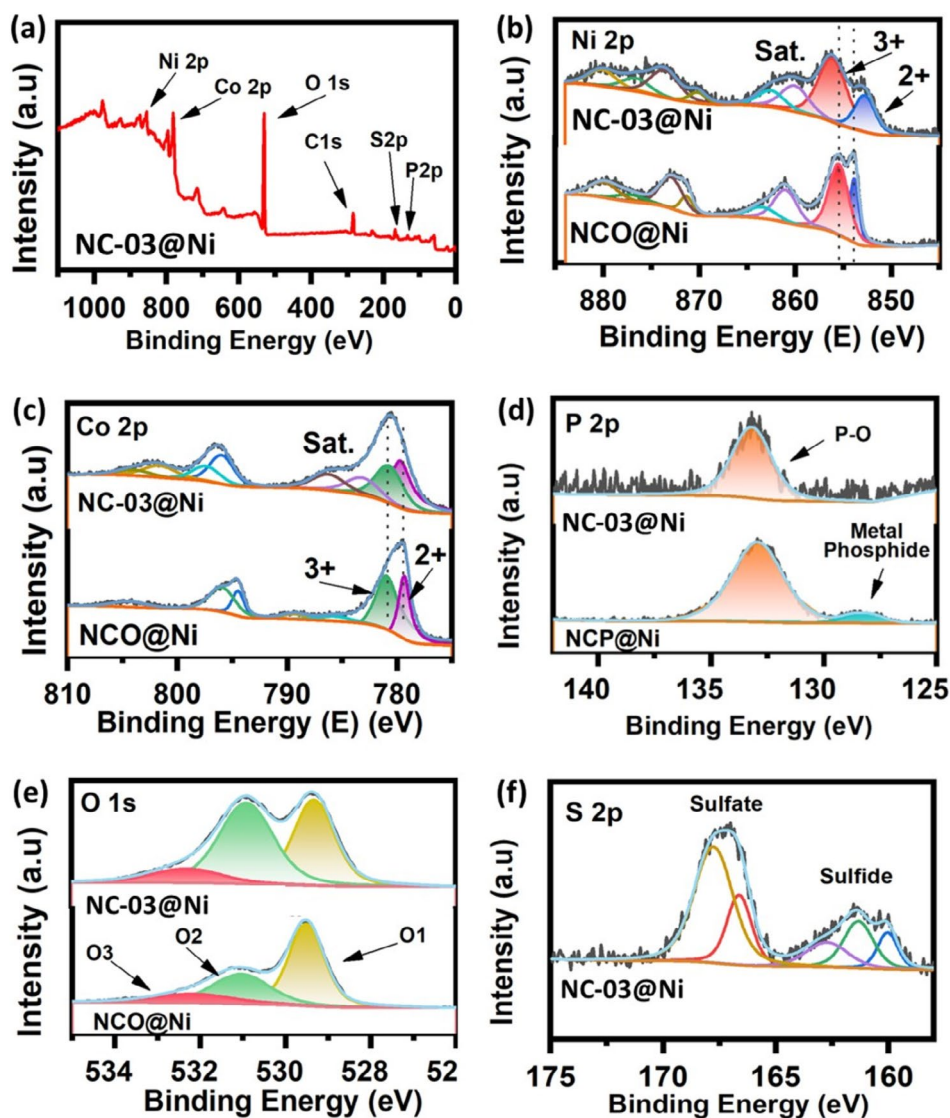


**FIGURE 4** | XPS (a) survey spectra of NC-3@Ni, and narrow spectra of (b) Ni 2p, (c) Co 2p, (d) P 2p, (e) O 1s, and (f) S 2p.

conducted at a rate of  $0.2 \text{ mVs}^{-1}$  within the voltage window of 2.0–4.5 V. All catalytic cathodes indicate ORR and OER activities during the respective cathodic and anodic cycles. CV studies reveal possibly the most conductive phases of all, the phosphide phases are highly electrochemically active, where the respective reduction and oxidation peaks of NCP@Ni presented at 2.23 and 4.05 V were found to be least shifted from the equilibrium of 2.96 V. Overall, the weakest activity was provided by the NCO@Ni, and the peak positioning and the current density of NCS@Ni was marginally better, compared with NCO@Ni. The heterogeneous cathode provided improved catalytic activity compared with pure oxide and sulfide counterparts, and its peak current densities and peak positioning were only second to the NCP@Ni. The oxidation peak present at 3.47 V, in addition to the peak at 4.24 V in NC-3@Ni, indicates the early decomposition of amorphously form  $\text{Li}_{2-x}\text{O}_2$  [11], which could be beneficial during the LOB operation to achieve lower charging overpotential under a limited discharge depth.

The low contact and interfacial resistance are essential for efficient and durable battery operation. The bottom-up crystal growth approach is known for engineering catalytic cathodes

with superior interfacial properties compared with the tape-casted electrodes with non-conductive binders [32]. As anticipated, all the derived self-standing catalytic electrodes exhibited a small series ohmic resistance during the EIS analysis conducted with 5 mV sinusoidal signals for a frequency range of 0.01–1000 Hz. The well-fitted equivalent circuits for the Nyquist plots provided in Figure 5b confirm the lowest series ohmic resistance ( $R_s$ ) of  $10.73 \Omega$  is provided by the NCP@Ni cathode-based LOB, while the hybrid, sulfide, and oxide cathodes provide, respectively, lower conductivities with the highest  $R_s$  of  $12.65 \Omega$  was reported by the NCO@Ni-based system. Alike  $R_s$ , the charge transfer resistance ( $R_{ct}$ ), which were calculated by the diameter of the semi-circle, was also found to follow the same order, where the lowest initial charge transfer resistance of  $178.20 \Omega$  was provided by the NCP@Ni cathode. The observations align closely with the results of the cyclic voltammetric analysis, where the NCP@Ni cathode exhibited the lowest polarization and highest current densities, followed by the NC-3@Ni cathode.

As illustrated in Figure 5c, GCD profiles of the assembled batteries with different self-standing catalytic cathodes were analyzed to reveal the depth of maximum discharge and the decomposition

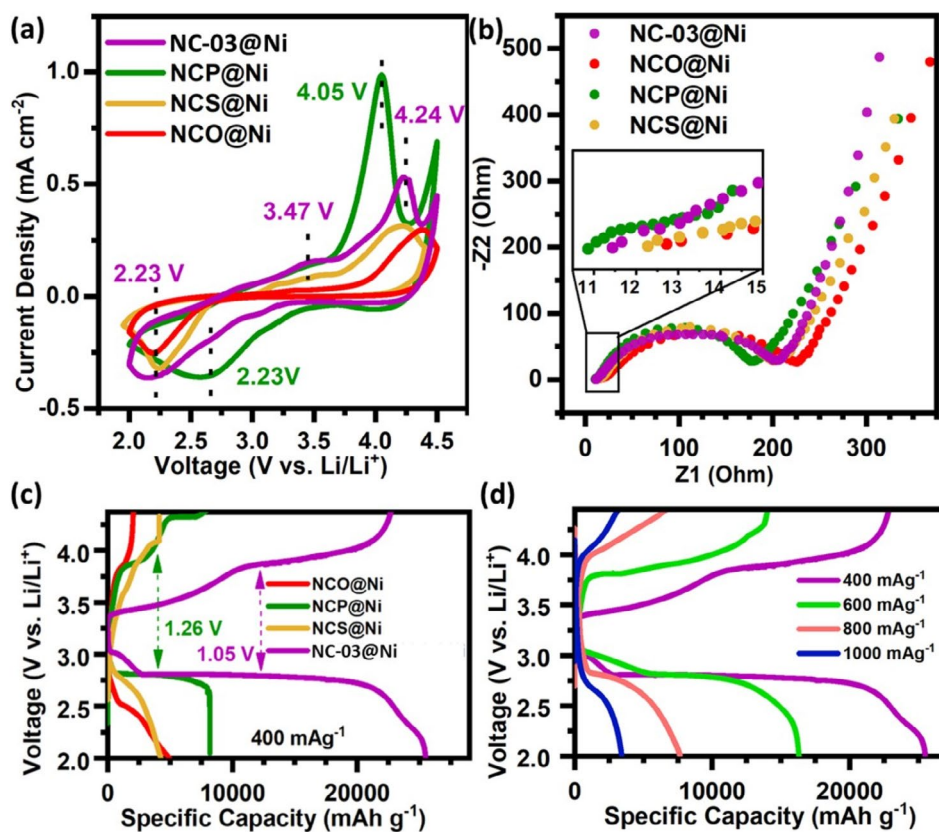


**FIGURE 5** | Electrochemical performances of different catalytic cathodes in the assembled LOBs: (a) cyclic voltammetry study conducted at scan rate  $0.2\text{ mV s}^{-1}$  in between 2.0 and 4.5 V, (b) EIS analysis of LOBs prior operation, (c) specific discharge/charge capacity at  $400\text{ mA g}^{-1}$ , (d) specific discharge/charge capacity of NC-3@Ni cathode-based LOB under different current densities.

capabilities at  $400\text{ mA g}^{-1}$  under the voltage window of 2.0–4.5 V. During the study, exceptionally good initial specific discharge capacity was shown by the LOB assembled with the hybrid cathode of NC-3@Ni, showing  $25\,162\text{ mAh g}^{-1}$  discharge capacity. The battery was able to well decompose the discharge product by achieving a specific charging capacity of  $22\,590\text{ mAh g}^{-1}$ , which is roughly 90% of the discharge capacity. In comparison, the LOBs with NCP@Ni, NCS@Ni, and NCO@Ni were only able to achieve the respective specific discharge/charge capacities of  $8030/7916$ ,  $4910/4892$ ,  $5068/2493\text{ mAh g}^{-1}$ . The highest capacities achieved by the catalysts with homogeneous phases were less than 1/3rd of the initial capacities achieved by the heterogeneous catalyst system, showcasing the superiority of the NC-3@Ni cathode-based LOBs operating under high current densities as  $400\text{ mA g}^{-1}$ . The measured charging overpotential of 1.05 V in NC-3@Ni cathode-based LOB is also the lowest, which is 0.21 V lower than the next best-performing cathode of NCP@Ni, verifying the stable catalytic performances in the heterogeneous catalyst. We reveal the morphology and the orientation of the discharge product are responsible for the greater charge storage performances, and the contribution of its surface charge distribution for the advantages of discharge product properties will be discussed in the following sections. The heterogeneous catalyst produced healthy discharge/charge capacities even as the current rate increased considerably as depicted in Figure 5d, showcasing the capabilities of the heterogeneous catalyst to adapt at faster reaction kinetics. The specific discharge/charge capacities were reported as  $16\,730/14\,085$ ,  $7510/6376$ ,  $3128/2819\text{ mAh g}^{-1}$  at respective current rates of 600, 800, and  $1000\text{ mA g}^{-1}$ , indicating

the heterogeneous catalyst can deliver similar capacitive depths at twice higher current rates, compared with the second-best performing catalyst of NCP@Ni.

Further delving into the electrocatalytic activities, the cycle performance of the assembled LOBs with the heterogeneous and the individual catalyst phases were studied under a current density of  $400\text{ mA g}^{-1}$  with a limited discharge capacity of  $1000\text{ mAh g}^{-1}$ .

Figure 6a depicts overlapped voltage-time profiles of the studied LOBs. In which, by far the longest cycle stability was provided by the NC-3@Ni heterogeneous cathode-based LOB, surviving over 1350 h of continuous operation. The heterogeneous LOB system provides a steady performance with a small overpotential of around 0.7 V and 100% coulombic efficiency throughout its operation of 270 cycles, without any noticeable signs of degradation, where Figure 6d,e provides information on the selected discharge/charge cycles during NC-3@Ni catalyst-based LOB operation and the energy efficiency during the LOB operation, respectively. Following the trend observed during the deep-discharge studies, the LOB assembled with bimetallic phosphide cathode delivered the second-best cycle performances. The NCP@Ni cathode-based LOB was active for a continuous 675 h operation, completing 137 cycles, before reaching the threshold conditions. The battery performances started to deteriorate after the first 200 h (40 cycles) of steady operation as indicated in Figure 6a, which is verified as the charging overpotential of 0.95 V observed after 50 cycles jumped to 1.15 V by the



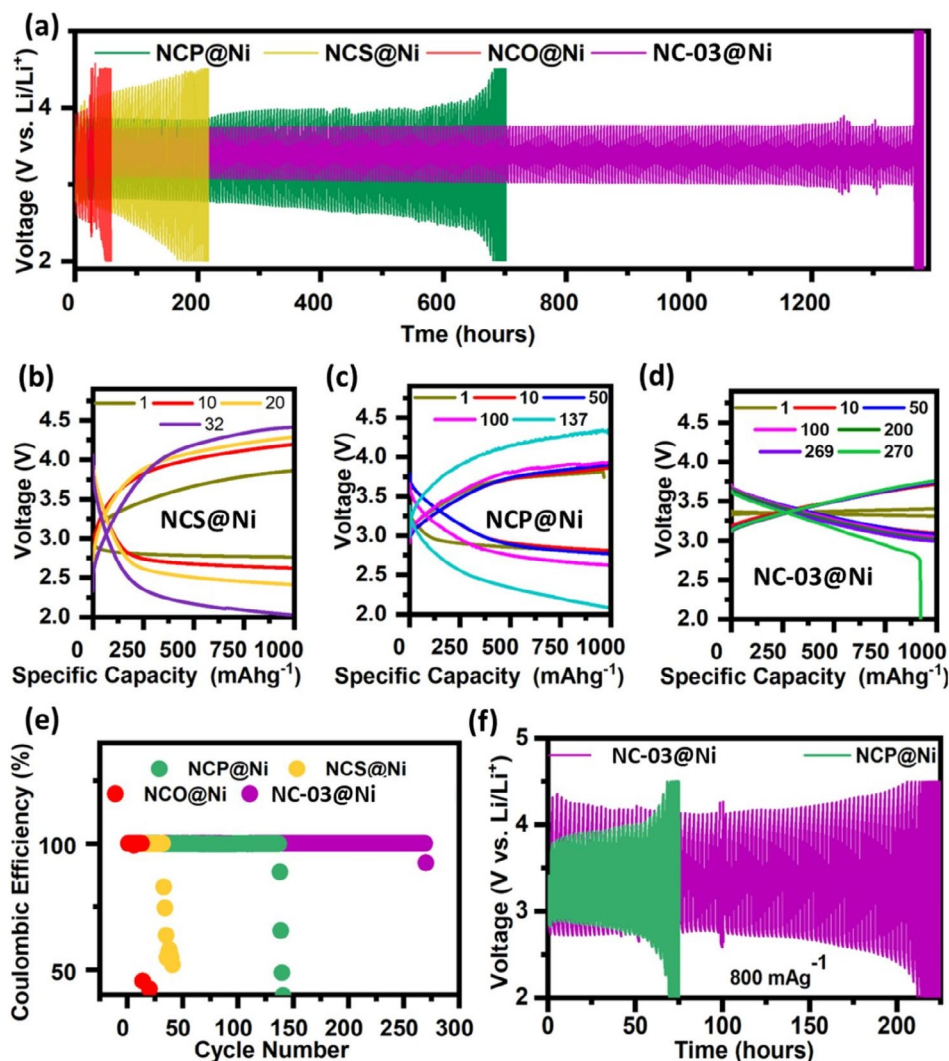


**FIGURE 6** | (a) Voltage versus time profile of different catalytic cathodes, selected cycles of (b) NCS@Ni, (c) NCP@Ni, (d) NC-3@Ni cathode-based LOBs, (e) Coulombic efficiency during the cycling process conducted at a rate of 400 mA g<sup>-1</sup> under a limited discharge depth of 1000 mAh g<sup>-1</sup> (f) Voltage versus time profile of heterogeneous and NCP@Ni cathode-based LOBs cycled at 800 mA g<sup>-1</sup> under a limited discharge depth of 1000 mAh g<sup>-1</sup>.

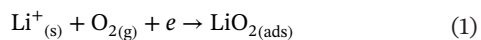
100th cycle, as observed in Figure 6c. These observations imply that even the best-performing individual catalyst of NiCoP is struggling to reach the designated discharge depths and the decomposition of the discharge products without considerable overpotential rises over 50 cycles.

Comparatively, weak catalyst phases of NiCo<sub>2</sub>S<sub>4</sub> and NiCo<sub>2</sub>O<sub>4</sub> identified during the CV studies were only able to survive 32 and 17 cycles, respectively, with the full energy efficiency. Inherent low conductivity in the transition metal oxide and sulfide phases [28] could also account for the sluggish kinetics display by the NCO@Ni and the NCS@Ni (see Figure 6b), as those catalysts failed to deliver under a current density as high as 400 mA g<sup>-1</sup>. The superior cyclic performance of the heterogeneous phases-based cathode was verified again as the cyclic capabilities of the LOBs were assessed under an increased current density (800 mA g<sup>-1</sup>). As exhibited in Figure 6e, the NC-3@Ni cathode-based LOB survived for 213 h completing 85 cycles with a 100% coulombic efficiency, while the NCP@Ni cathode-based LOB was only able to last 28 cycles operating for 71 h.

Over the years, most of the arguments were against the suitability of cathodic solid electrocatalysts, citing the catalysts will become inaccessible and useless as a film-like discharge product grows on top of the cathode surface, covering the catalytic sites [7, 33]. However, the electrochemical performances of the heterogeneous triphase catalyst have shown considerably improved outcomes, overcoming the key limitations identified with the single-structure catalysts. We believe the swift charge transfers between the heterogeneous phases as identified during the XPS studies are playing a pivotal role in the enhanced catalytic performances, and its impact on the discharge product morphology and orientation is discussed using the SEM images of the disassembled LOB cathode as presented in Figure 7, obtained once the batteries were fully discharged at 400 mA g<sup>-1</sup>.

The SEM images of the disassembled battery cathodes obtained after the full discharge provide invaluable information on the battery discharging mechanism. During the LOB discharge, initially, O<sub>2</sub> gas diffusing into the battery will electrochemically

reduce at the surface of the cathode forming an unstable discharge product of  $\text{LiO}_2$ , as presented in the following equation [3].



The solid electrocatalysts tend to keep the intermediate discharge product and the final discharge product of  $\text{Li}_2\text{O}_2$  to the surface of the cathode, irrespective of the formation mechanism of  $\text{Li}_2\text{O}_2$ , either through the more common reaction pathway of

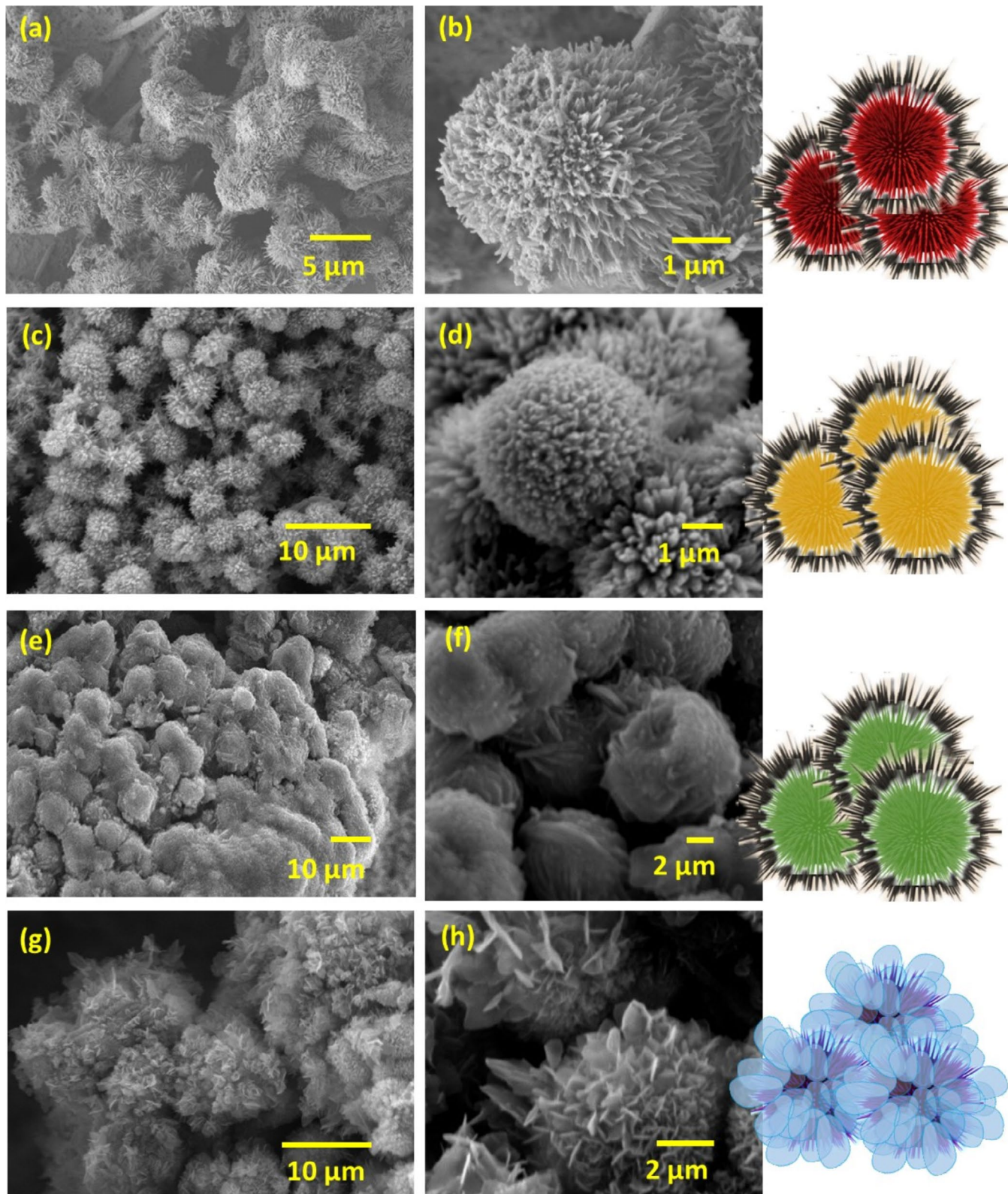
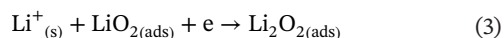
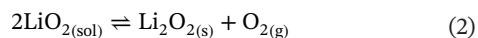


**FIGURE 7** | SEM images of discharged LOB cathodes and relevant graphical representations of (a, b) NCO@Ni, (c, d) NCS@Ni, (e, f) NCP@Ni, and (g, h) heterogeneous cathode of NC-3@Ni.

disproportionation (see Equation 2) or through a second electrochemical reduction as indicated in Equation (3) [3].



Once the produced  $\text{Li}_2\text{O}_2$  stays well-attached to the surface, it grows as a surface coating covering the surface of the cathode. Previous studies concluded that porosity and the electrical conductivity of the cathode reduce as the thickness of the  $\text{Li}_2\text{O}_2$  layer increases, and the cathode surface becomes mostly passivated once the  $\text{Li}_2\text{O}_2$  layer becomes 9 nm thick, terminating the further discharge [34]. In such scenarios, the volumetric discharge capacities achieved are rather limited, even though the LOBs could charge with relatively lower overpotentials compared with the ones using redox mediators since the discharge product is kept well intact with the surface of the cathode. Hence, irrespective of the catalytic activity, the discharge depths that could be achieved by a solid electrocatalyst were limited, which makes an indistinct future for solid electrocatalysts in LOBs. In addition to the previously discussed cycle stability and discharge capacity studies, the observation made during the SEM studies mostly followed up with the above-mentioned rationale. Because the catalytic particles provide a similar catalytic activity throughout the catalytic microstructure, NCO@Ni supports the growth of a film-like discharge product morphology forming a coating covering the surface of the cathode, as depicted in Figure 7a,b, including a graphical representation of surface coating of  $\text{Li}_2\text{O}_2$  (black) covering the catalytic particles, represents in red color. Unsurprisingly, similar morphological features were presented by the discharge cathode of NCS@Ni, which also confirms the growth of a film-like  $\text{Li}_2\text{O}_2$  as presented in Figure 7c,d. Even

though the NCP@Ni cathode acquired a thicker coverage of  $\text{Li}_2\text{O}_2$  upon discharge, mostly due to better conductivity and better catalytic activity, the growth mechanism of the discharge product was still the same as displayed in Figure 7e,f. However, a different discharge product morphology was observed in the NC-3@Ni discharge battery cathode, which is a slightly curved sheet-like structure, grown parallel to the surface of the cathode as presented in Figure 7g,h with relevant graphical illustrations. Unlike a similar catalytic activity observed throughout the microstructure in homogeneous catalytic phases, the identified heterogeneous phases of NiCoP,  $\text{NiCo}_2\text{S}_4$ , and  $\text{NiCo}_2\text{O}_4$  have produced a different catalytic activity in individual domains, producing a non-homogenous catalytic activity within the heterogeneous catalyst microstructures, which continues throughout the hierarchical network. Herein, certain high conductive and electron-rich domains such as NiCoP could provide additional support for oxygen reduction by acting as local nucleophilic domains, while the inherently low conductive metal oxide domains as  $\text{NiCo}_2\text{O}_4$  could promote the decomposition of the  $\text{Li}_2\text{O}_2$  by acting as local electrophilic domains, as previous reports suggest [17, 23]. Hence, the growth of the discharge product was not uniform throughout the catalytic surface, and the induced local electric fields from the local charge concentrated domains toward the local charge deficient domains could ensure a fast charge transport while modulating the surface electron structure as observed during the XPS studies.

The respective ex-situ Raman and XRD spectroscopies of the discharged and charged cathodes provided in Figures S4 and S5 further verified the formation of  $\text{Li}_2\text{O}_2$  during the discharge, and the full decomposition of it upon charging, confirming the successful operation of the tri-phase heterogeneous cathode-based LOBs. Upon discharge, the appearance of the

**TABLE 1** | The electrochemical performance of the Li-O<sub>2</sub> battery using the triphase heterogeneous catalyst (NC-3@Ni), in comparison with alternatives extracted from the literature.

Catalyst	Discharge capacity (mAhg <sup>-1</sup> )	Current density (mAg <sup>-1</sup> )	Number of cycles	Current density (mAhg <sup>-1</sup> )	Discharge product morphology
RuO <sub>2</sub> [9]	7900	300	173	300	Film
NiCoFeO [12]	16727	100	197	500	Film
NiCoP [38]	9320	100	150	500	Film
Ag <sub>2</sub> Mo <sub>2</sub> O <sub>7</sub> [39]	15898	500	817	500	Film
CoSe <sub>2</sub> @NiSe <sub>2</sub> [22]	3530	100	60	100	Flower-like
Ni-Co-Fe-O [40]	3111	50	125	50	—
NiCo <sub>2</sub> S <sub>4</sub> @NiO [21]	10050	200	300	200	Peasecod-like
Fe-RuO <sub>2</sub> [41]	23628	200	134	200	Toroid and Sheet
Mn <sub>2</sub> O <sub>3</sub> [42]	21070	500	180	500	Film
2D Ti <sub>0.87</sub> O <sub>2</sub> /MXene [43]	11120	200	407	200	Film
CoP/Co <sub>2</sub> P [28]	14632	100	161	200	Porous boxes
NiO@NiP [16]	18254	500	240	500	Sheet-like
<b>NC-3@Ni</b>	<b>25162</b>	<b>400</b>	<b>270</b>	<b>400</b>	<b>Sheet-like</b>

Note: Values in bold are related to the current study.

peaks at 261 and 796  $\text{cm}^{-1}$  in the Raman spectra confirmed the formation of  $\text{Li}_2\text{O}_2$  [35]. The detection of sharp peaks of  $\text{Li}_2\text{O}_2$  indicates the less-crystalline nature of the discharged product, whereas the shorter O–O bond length and the comparably defective nature in less crystalline nature (compared with toroidal  $\text{Li}_2\text{O}_2$ ) make it easily detectable with Raman spectroscopy [36]. The initial cathode of NC-3@Ni was free from any apparent peak in the area of interest, while a peak around 710–730  $\text{cm}^{-1}$  appeared in all of the tested battery cathodes, which is assignable to  $[\text{TFSi}]^-$ , a residual peak from the electrolyte [37]. Importantly, the peaks associated with  $\text{Li}_2\text{O}_2$  were found to have disappeared from the charged cathode, indicating a successful decomposition. The absence of any peak related to  $\text{LiOH}$  or  $\text{Li}_2\text{CO}_3$  helps to conclude that the minimal side reactions occurred during the LOB operation, and their presence could trigger a premature death of the battery. As expected, some residual  $\text{Li}_2\text{O}_2$  was detected from the long-cycled cathode after 100 cycles, indicating the typical aging of the catalyst. Compared with the RAMAN study, the ex-situ XRD study has less clarity. The strong signals from the Ni foam and the void full rough morphology of the electrode surface make ex-situ XRD analysis more challenging. However, the disappearance of the peaks presented at  $2\theta = 21.4, 31.9, 34.2,$  and  $59.1$  on the discharged cathode assignable to  $\text{Li}_2\text{O}_2$  (JCPDS 01-073-1640) from the charged cathode as presented in Figure S4, suggests the successful decomposition of the discharge product from the NC-3@Ni cathode upon charging.

The observations made during the ex-situ SEM study of the discharged cathode of NC-3@Ni heterogeneous cathode further justified the observations made during the electrochemical studies. Unlike a film-like layer, the parallelly grown sheet-like morphology of the discharge product will not block the Li-ion diffusion into the cathode or passivate the catalyst sites, in favor of achieving a higher discharge depth as reported, more than 3 times over the studied homogeneous catalyst phases. Furthermore, the presence of heterogeneous phases overcomes the reaction kinetic limitations that could occur in the systems with individual phases, allowing the LOBs to perform well in higher current densities. Essentially, since the produced  $\text{Li}_2\text{O}_2$  deposited in contact with the battery cathode, significantly low charging overpotentials were reported, allowing the constructed LOB system to outperform the homogeneously distributed single catalyst systems and dual-phase heterogeneous catalyst systems reported in recent years as presented in Table 1.

## 4 | Conclusion

In summary, we have synthesized and integrated a triphase heterogeneous catalytic microstructure as the  $\text{O}_2$  cathode in LOB. The catalyst material comprises the domains of binary oxide, sulfide, and phosphide phases of NiCoP,  $\text{NiCo}_2\text{S}_4$ , and  $\text{NiCo}_2\text{O}_4$  within the hollow microstructures, which are assembled in a hierarchical order on Ni foam. While the hollow core benefits in achieving higher gravimetric performances, the major contribution was made by the heterogeneous phases towards the superior LOB performances, by modulating the discharge product morphology and the orientation. The phases with different

electronic properties were found to be promoting the growth of sheet-like  $\text{Li}_2\text{O}_2$ , assembled vertically on the cathode surface. The mechanism advocates fast reaction kinetics, higher discharge depths, and longer cyclability, where the heterogeneous catalytic cathode-based LOB achieved 25162  $\text{mAhg}^{-1}$  of first discharge capacity at 400  $\text{mA}g^{-1}$ , and 270 cycles at 400  $\text{mA}g^{-1}$  under a limited discharge depth of 1000  $\text{mAhg}^{-1}$ , exceeding 1350 h of continuous operation. In comparison, the NiCoP-used cathode-based LOB performed best among the individual catalytic structures explored on the heterogeneous catalytic system. However, the performances of NiCoP are less than one-third and half of the produced respective specific capacity and cyclability by the heterogeneous catalyst-based LOBs, exhibiting the effectiveness in the explored strategy.

## Author Contributions

**Shadeepa Karunarathne:** Conceptualization, Methodology, Investigation, Formal analysis, Visualization, Writing – original draft. **Chanaka Sandaruwan:** Investigation, Visualization, **Yasun Y. Kannangara:** investigation, visualization. **Denisa Demko:** Investigation, Visualization, **Francois Orange:** Investigation, Visualization. **Alica Mija:** Funding acquisition, Resources, Writing – review and editing. **Ali Reza Kamali:** Resources, Supervision, Funding acquisition, Conceptualization, Writing – review and editing. **Amr M. Abdelkader:** Resources, Supervision, Funding acquisition, Conceptualization, Writing – review and editing.

## Acknowledgments

This work has been supported by the French government, through the UCAJ.E.D.I. Investments in the Future project managed by the National Research Agency (ANR) with the reference number ANR-15-IDEX-01. Financial support from National Natural Science Foundation of China (52250610222) is appreciated.

## Conflicts of Interest

The authors declare no conflicts of interest.

## References

1. R. Wang, B. Weng, A. Mahadevegowda, et al., “Influence of Carbonate Electrolyte Solvents on Voltage and Capacity Degradation in Li-Rich Cathodes for Li-Ion Batteries,” *Advanced Energy Materials* 14 (2024): 2401097.
2. J. B. Robinson, K. Xi, R. V. Kumar, et al., “2021 Roadmap on Lithium Sulfur Batteries,” *Journal of Physics: Energy* 3 (2021): 031501.
3. S. Karunarathne, C. K. Malaarachchi, A. M. Abdelkader, and A. R. Kamali, “Advances in Bifunctional Electrocatalysts Towards High-Performing Li-Air Batteries,” *Journal of Power Sources* 607 (2024): 234553.
4. T. Liu, X.-Y. Yang, and X.-B. Zhang, “Recent Progress of Flexible Lithium-Air/ $\text{O}_2$  Battery,” *Advanced Materials Technologies* 5 (2020): 2000476.
5. A. Samojlov, D. Schuster, J. Kahr, and S. A. Freunberger, “Surface and Catalyst Driven Singlet Oxygen Formation in Li- $\text{O}_2$  Cells,” *Electrochimica Acta* 362 (2020): 137175.
6. B. Scrosati, “The Lithium Air Battery: Fundamentals. Edited by Nobuyuki Imanishi, Alan C. Luntz, and Peter G. Bruce,” *Angewandte Chemie, International Edition* 54 (2015): 5554.
7. W. J. Kwak, D. Sharon, C. Xia, et al., “Lithium–Oxygen Batteries and Related Systems: Potential, Status, and Future,” *Chemical Reviews* 120, no. 14 (2020): 6626–6683, <https://doi.org/10.1021/acs.chemrev.9b00609>.

8. C. Prehal, S. Mondal, L. Lovicar, and S. A. Freunberger, "Exclusive Solution Discharge in Li-O<sub>2</sub> Batteries?," *ACS Energy Letters* 7 (2022): 3112–3119.
9. Y. Dou, X. G. Wang, D. Wang, et al., "Tuning the Structure and Morphology of Li<sub>2</sub>O<sub>2</sub> by Controlling the Crystallinity of Catalysts for Li-O<sub>2</sub> Batteries," *Chemical Engineering Journal* 409 (2021): 128145.
10. M. Kim, H. Lee, H. J. Kwon, et al., "Carbon-Free High-Performance Cathode for Solid-State Li-O<sub>2</sub> Battery," *Science Advances* 8 (2022): 8584.
11. S. Karunarathne, Y. Y. Kannangara, C. R. Ratwani, et al., "Stoichiometrically Optimized Egorbital Occupancy of Ni-Co Oxide Catalysts for Li-Air Batteries," *Nanoscale* 16 (2024): 7937–7950.
12. L. Ren, R. Zheng, D. Du, et al., "Optimized Orbital Occupancy of Transition Metal in Spinel Ni-Co Oxides With Heteroatom Doping for Aprotic Li-O<sub>2</sub> Battery," *Chemical Engineering Journal* 430 (2022): 132977.
13. X. Luo, L. Ge, L. Ma, et al., "Effect of Componential Proportion in Bimetallic Electrocatalysts on the Aprotic Lithium-Oxygen Battery Performance," *Advanced Energy Materials* 8, no. 20 (2018): 1703230, <https://doi.org/10.1002/aenm.201703230>.
14. N. C. Lai, G. Cong, Z. Liang, and Y. C. Lu, "A Highly Active Oxygen Evolution Catalyst for Lithium-Oxygen Batteries Enabled by High-Surface-Energy Facets," *Joule* 2 (2018): 1511–1521.
15. C. Xiao, B. A. Lu, P. Xue, et al., "High-Index-Facet- and High-Surface-Energy Nanocrystals of Metals and Metal Oxides as Highly Efficient Catalysts," *Joule* 4 (2020): 2562–2598.
16. Y. Yan, Z. Ran, T. Zeng, et al., "Interfacial Electron Redistribution with Hydrangea-Like NiO@Ni<sub>2</sub>P Heterogeneous Microspheres With Dual-Phase Synergy for High-Performance Lithium-Oxygen Battery," *Small* 18, no. 10 (2022): 2106707, <https://doi.org/10.1002/sml.202106707>.
17. Q. Xia, D. Li, L. Zhao, et al., "Recent Advances in Heterostructured Cathodic Electrocatalysts for Non-Aqueous Li-O<sub>2</sub> Batteries," *Chemical Science* 13 (2022): 2841–2856.
18. D. Ma, B. Hu, W. Wu, et al., "Highly Active Nanostructured CoS<sub>2</sub>/CoS Heterojunction Electrocatalysts for Aqueous Polysulfide/Iodide Redox Flow Batteries," *Nature Communications* 10 (2019): 1.
19. H. Wang, K. Xie, Y. You, et al., "Realizing Interfacial Electronic Interaction Within ZnS Quantum Dots/N-rGO Heterostructures for Efficient Li-CO<sub>2</sub> Batteries," *Advanced Energy Materials* 9 (2019): 1901806.
20. T. Liu, A. Li, C. Wang, W. Zhou, S. Liu, and L. Guo, "Interfacial Electron Transfer of Ni<sub>2</sub>P-NiP<sub>2</sub> Polymorphs Inducing Enhanced Electrochemical Properties," *Advanced Materials* 30, no. 46 (2018): 1803590, <https://doi.org/10.1002/adma.201803590>.
21. P. Wang, C. Li, S. Dong, et al., "Hierarchical NiCo<sub>2</sub>S<sub>4</sub>@NiO Core-Shell Heterostructures as Catalytic Cathode for Long-Life Li-O<sub>2</sub> Batteries," *Advanced Energy Materials* 9 (2019): 1900788.
22. R. Liang, C. Shu, A. Hu, et al., "Interface Engineering Induced Selenide Lattice Distortion Boosting Catalytic Activity of Heterogeneous CoSe<sub>2</sub>@NiSe<sub>2</sub> for Lithium-Oxygen Battery," *Chemical Engineering Journal* 393 (2020): 124592.
23. C. Wu, Y. Hou, J. Jiang, et al., "Heterostructured Mo<sub>2</sub>C-MoO<sub>2</sub> as Highly Efficient Catalyst for Rechargeable Li-O<sub>2</sub> Battery," *Journal of Power Sources* 470 (2020): 228317.
24. Y. Y. Kannangara, S. Karunarathne, W. P. S. L. Wijesinghe, et al., "The Electrochemical Performance of Various NiCo<sub>2</sub>O<sub>4</sub> Nanostructures in Hybrid Supercapacitors: Investigating the Impact of Crystalline Defects," *Journal of Energy Storage* 84 (2024): 110717.
25. H. Xie, D. Jiang, H. Chen, et al., "Electron Transfer and Surface Activity of NiCoP-Wrapped MXene: Cathodic Catalysts for the Oxygen Reduction Reaction," *Nanoscale* 15 (2023): 7430–7437.
26. W. Liu, J. Zhang, Z. Bai, et al., "Controllable Urchin-Like NiCo<sub>2</sub>S<sub>4</sub> Microsphere Synergized With Sulfur-Doped Graphene as Bifunctional Catalyst for Superior Rechargeable Zn-Air Battery," *Advanced Functional Materials* 28 (2018): 1706675.
27. K. Bhunia, M. Chandra, S. Kumar Sharma, D. Pradhan, and S. J. Kim, "A Critical Review on Transition Metal Phosphide Based Catalyst for Electrochemical Hydrogen Evolution Reaction: Gibbs Free Energy, Composition, Stability, and True Identity of Active Site," *Coordination Chemistry Reviews* 478 (2023): 214956.
28. M. Li, M. Yuan, X. Zheng, et al., "Highly Polar CoP/Co<sub>2</sub>P Heterojunction Composite as Efficient Cathode Electrocatalyst for Li-Air Battery," *Chinese Chemical Letters* 35 (2023): 109265.
29. X. Zhang, J. Wang, Y. Bi, et al., "Innovative Catalyst Design of Sea-Urchin-Like NiCoP Nanoneedle Arrays Supported on N-Doped Carbon Nanospheres for Enhanced HER Performance," *Langmuir* 40 (2024): 5518–5526.
30. Y. Y. Kannangara, P. Prabunathan, and J. K. Song, "Facile Synthesis of a Hierarchical CuS/CuSCN Nanocomposite With Advanced Energy Storage Properties," *New Journal of Chemistry* 42 (2018): 15387–15396.
31. Y. Z. Liu, T. Chen, Q. Zhang, and R. Y. Jiang, "A Simple Hydrothermal Synthesis of Flower-Like NiCo<sub>2</sub>S<sub>4</sub>@ Biomass-Graded Porous Carbon With Structural Synergy and Excellent Capacitive Performance," *ChemistrySelect* 7 (2022): e202200361.
32. D. A. Agyeman, M. Park, and Y. M. Kang, "Pd-Impregnated NiCo<sub>2</sub>O<sub>4</sub> Nanosheets/Porous Carbon Composites as a Free-Standing and Binder-Free Catalyst for a High Energy Lithium-Oxygen Battery," *Journal of Materials Chemistry A* 5 (2017): 22234–22241.
33. G. A. Attard, P. G. Bruce, E. J. Calvo, et al., "Mechanism of ORR and OER in Non-Aqueous Electrolytes: General Discussion," *Faraday Discussions* 248 (2024): 210–249.
34. H. C. Lee, J. O. Park, M. Kim, et al., "High-Energy-Density Li-O<sub>2</sub> Battery at Cell Scale With Folded Cell Structure," *Joule* 3 (2019): 542–556.
35. F. S. Gittleson, K. P. C. Yao, D. G. Kwabi, et al., "Raman Spectroscopy in Lithium-Oxygen Battery Systems," *ChemElectroChem* 2 (2015): 1446–1457.
36. S. Ma, L. Sun, L. Cong, et al., "Multiporous MnCo<sub>2</sub>O<sub>4</sub> Microspheres as an Efficient Bifunctional Catalyst for Nonaqueous Li-O<sub>2</sub> Batteries," *Journal of Physical Chemistry C* 117 (2013): 25890–25897.
37. B. A. Fortuin, L. Meabe, S. R. Peña, et al., "Molecular-Level Insight Into Charge Carrier Transport and Speciation in Solid Polymer Electrolytes by Chemically Tuning Both Polymer and Lithium Salt," *Journal of Physical Chemistry C* 127 (2023): 1955–1964.
38. C. Dang, P. Feng, S. He, et al., "NiCoP Based Carbon Nanotube Heterostructure for Improved Oxygen Redox Reaction Kinetics in Li-O<sub>2</sub> Batteries," *Electrochimica Acta* 462 (2023): 142771.
39. H. Yu, G. Zhang, D. Zhang, et al., "Homogeneous In-Plane Lattice Strain Enabling d-Band Center Modulation and Efficient d-π Interaction for an Ag<sub>2</sub>Mo<sub>2</sub>O<sub>7</sub> Cathode Catalyst With Ultralong Cycle Life in Li-O<sub>2</sub> Batteries," *Advanced Energy Materials* 14 (2024): 2401509.
40. K. Adpakpang, S. M. Oh, D. A. Agyeman, et al., "Holey 2D Nanosheets of Low-Valent Manganese Oxides With an Excellent Oxygen Catalytic Activity and a High Functionality as a Catalyst for Li-O<sub>2</sub> Batteries," *Advanced Functional Materials* 28 (2018): 1707106.
41. Z. Lian, Y. Lu, S. Zhao, Z. Li, and Q. Liu, "Engineering the Electronic Interaction Between Atomically Dispersed Fe and RuO<sub>2</sub> Attaining High Catalytic Activity and Durability Catalyst for Li-O<sub>2</sub> Battery," *Advanced Science* 10 (2023): 2205975.

42. L. Zhao, J. Feng, A. Abbas, C. Wang, and H. Wang, "MOF-Derived  $\text{Mn}_2\text{O}_3$  Nanocage With Oxygen Vacancies as Efficient Cathode Catalysts for Li- $\text{O}_2$  Batteries," *Small* 19 (2023): 2302953.

43. D. Zhang, G. Zhang, R. Liu, et al., "Mutually Activated 2D  $\text{Ti}_{0.87}\text{O}_2$ /MXene Monolayers Through Electronic Compensation Effect as Highly Efficient Cathode Catalysts of Li- $\text{O}_2$  Batteries," *Advanced Functional Materials* 35 (2025): 2414679.

### Supporting Information

Additional supporting information can be found online in the Supporting Information section.